Atmospheric
Measurement
Techniques
Discussions

A low-cost mobile multidisciplinary measurement platform for monitoring geophysical parameters

1 Olivier F.C. den Ouden[1,2], Jelle D. Assink[1], Cornelis D. Oudshoorn[3] Dominique Filippi[4] and Läslo G. Evers[1,2]

2

3 [1]R&D Department of Seismology and Acoustics, Royal Netherlands Meteorological Institute, De Bilt, The Netherlands

4 [2]Dept. of Geoscience and Engineering, Delft University of Technology, Delft, The Netherlands

5 [3]R&D Department of Observations and Data Technology, Royal Netherlands Meteorological Institute, De Bilt, The Netherlands

6 [4]Sextant Technology Inc., Marton, New-Zealand

7

8 **Abstract**

9   Geophysical studies and real-time monitoring of natural hazards, such as volcanic eruptions or severe

10 weather events, benefit from the joint analysis of multiple geophysical parameters. However, typical

11 geophysical measurement platforms still provide logging solutions for a single parameter, due to different

12 community standards and the higher cost rate per added sensor.

13   In this work, the 'infrasound-logger' is presented, which has been designed as a low-cost mobile mul-

14 tidisciplinary measurement platform for geophysical monitoring. The platform monitors in particular

15 infrasound, but concurrently measures barometric pressure, accelerations, wind flow and uses the Global

16 Positioning System (GPS) for positioning of the platform. Due to its digital design, the sensor platform

17 can readily be integrated with existing geophysical data infrastructures and be embedded in the analysis of

18 geophysical data. The small dimensions and lower cost price per unit allow for unconventional experimen-

19 tal designs, for example high density spatial sampling or deployment on moving measurement platforms.

20 Moreover, such deployments can complement existing high-fidelity geophysical sensor networks. The

21 platform is designed using digital Micro-electromechanical Systems (MEMS) sensors that are embedded

22 on a Printed Circuit Board (PCB). The MEMS sensors on the PCB are: a GPS, a three-component

23 accelerometer, a barometric pressure sensor, an anemometer and a differential pressure sensor. A pro-

24 grammable microcontroller unit controls the sampling frequency of the sensors, and the data storage. A

25 waterproof casing is used to protect the mobile platform against the weather. The casing is created with

26 a stereolithography (SLA) Formlabs 3D printer, using durable resin.

27   Thanks to a low power consumption (9 Wh over 25 days), the system can be powered by a battery or

28 solar panel. Besides the description of the platform design, we discuss the calibration and performance

29 of the individual sensors.

Atmospheric
Measurement
Techniques

Open Access

EGU

Discussions

1   Introduction

Real-time monitoring of natural hazards, such as volcanic eruptions or severe weather events benefit from the joint analysis of multiple geophysical parameters. However, geophysical measurement platforms are typically designed for the measurement of a single parameter, due to different community standards and the higher cost rate per added sensor. The quality and robustness of geophysical measuring equipment generally scales with price, due to higher material costs and research and development (R&D) expenses of the manufacturer. In addition, the deployment of such equipment comes with complex deployment and calibration procedures, and requires the presence of a robust power and data infrastructure.

Geophysical institutes often place multiple sensor platforms co-located. Meteorological institutes, for example, measure various meteorological parameters for comparison, which improves the weather observations, as well as weather forecast models. The Comprehensive Nuclear-Test-Ban Treaty Organization (CTBTO) performs various geophysical measurements at its measurement sites where possible. The International Monitoring System (IMS), which is in place for the verification of the CTBT, performs continuous seismic, hydroacoustic, infrasonic and radionuclide measurements [Marty, 2019]. In addition, the IMS infrasound arrays and radionuclide facilities host auxiliary meteorological equipment, as this data facilitates the review of the primary IMS data streams. Besides its use for verifying the CTBT, it has also been shown that a multi-instrumental observation observational network such as the IMS can provide useful information on the vertical dynamic structure of the middle and upper atmosphere, in particular when paired with complementary upper atmospheric remote sensing techniques such as lidar [Blanc et al., 2018]. Other studies that involve the analysis of multiple geophysical parameters include seismo-acoustic analyses of explosions ([Assink et al., 2018] [Averbuch et al., 2020]), earthquakes ([Shani-Kadmiel et al., 2018]), and volcanoes ([Green et al., 2012]).

National Weather Services, such as the Royal Netherlands Meteorological Institute (KNMI), have expressed an interest in measuring weather on a local scale to inform citizens and warn in case of extreme weather. In addition, such measurements allow for higher-resolution measurements of sub-grid scale atmospheric dynamics, which will contribute the improvement of short-term and now-casting weather forecasts. Therefore it became part of a low-cost citizen weather station program, to increase the spatial resolution of conventional

numerical weather prediction models. In the Netherlands, over 300 of those weather stations are contributing to a global citizen science project, Weather Observations Website (WOW)[Garcia-Marti et al., 2019] [Cornes et al., 2020]. Nonetheless, due to the required infrastructure of the equipment, many platforms are spatially static. Having a low-cost multidisciplinary mobile sensor platform allows for high-resolution spatial sampling and complement existing high-fidelity geophysical sensor networks [Poler et al., 2020].

Various disciplines are applying new sensor technology to obtain higher spatial and temporal resolution [D'Alessandro et al., 2014] for geophysical hazard monitoring. Micro-electromechanical systems (MEMS) are small single-chip sensors that combine electrical and mechanical components and have a low energy consumption. The seismic community has created low-cost reliable MEMS accelerometers [Homeijer et al., 2011] [Milligan et al., 2011] [Zou et al., 2014] to detect strong accelerations that exceed values due to Earth's gravity field [Speller and Yu, 2004] [Laine and Mougenot, 2007] [Homeijer et al., 2014]. Moreover, the infrasound [Marcillo et al., 2012] [Anderson et al., 2018], as well as the meteorological community are integrating MEMS sensors into the existing sensor network [Huang et al., 2003] [Fang et al., 2010] [Ma et al., 2011].

In this work, the 'infrasound-logger' is presented, which has been designed as a low-cost mobile multidisciplinary measurement platform for geophysical monitoring, in particular, infrasound. The platform uses various digital MEMS sensors, which are embedded on a Printed Circuit Board (PCB). A programmable microcontroller unit, as well embedded on the PCB, controls the sampling frequency of the sensors and establishes the energy supply for the sensors as well as the data-communication and storage. A waterproof casing protect the mobile platform against weather. The casing is created with a stereo-lithography (SLA) Formlabs 3D printer, using durable resin. Because of it's low power consumption, the system can be powered by a battery or solar panel.

The ability to detect infrasonic signals of interest depends on the strength of the signal relative to the noise levels at the receiver side, the signal to noise ratio (SNR). The signal strength depends on the transmission loss that a signal experiences propagating from source to receiver. Infrasound measurements benefits from insights in the atmospheric noise levels (e.g., wind conditions), the meteorological conditions (e.g., barometric pressure, temperature, and humidity), as well as the movement and positioning of the sensors (e.g., accelerations) [Evers, 2008].

83 While there are clear benefits associated with a MEMS-based mobile platform (e.g., cheap and rapid de-

84 ployments to (temporarily) increase coverage), MEMS sensors are known to be less accurate than con-

85 ventional high-fidelity equipment. Especially digital MEMS sensors, which have a build-in Analog-Digital-

86 Converter (ADC), are known for their high self-noise level. Nonetheless, they could be used near a geo-

87 physical sources which generate high SNR signals. Several geophysical measurements [Marcillo et al., 2012]

88 [Grangeon and Lesage, 2019] [Laine and Mougenot, 2007] [D'Alessandro et al., 2014] show the benefit of MEMS

89 sensors, and how they complement the existing sensor network.

90 In this paper, the design and calibration of the 'infrasound-logger' is discussed. Due to its digital design, the

91 platform can readily be integrated in existing geophysical sensor infrastructures. The remainder of this article

92 is organized as follows. Section 2 introduces the mobile platform, its design and features. Section 3 describes

93 the various sensor that are embedded on the platform as well as the relative calibrations with high-fidelity

94 reference equipment. Firstly, a novel miniature digital infrasound sensor is introduced and its theoretical

95 response is derived. Secondly, the barometric MEMS sensor is discussed. A novel wind sensor which relies on

96 thermo-resistive elements is discussed next, followed by a discussion of the on-board MEMS accelerometer.

97 In Section 4 the overall performance and design of the platform are discussed and summarized, from which

98 the conclusions are drawn.

99 2 Mobile platform design

100 2.1 Circuit design

101 The mobile platform contains a PCB, which been created to embed the MEMS sensors and to facilitate

102 the electrical circuits. The PCB carries a Digital Low Voltage Range (DLVR) differential pressure sensor,

103 an anemometer, as well as an accelerometer and barometeric pressure sensor, in addition to a GPS for

104 location and timing purposes (Figure 1-a). The sensors are controlled by a MSP430 microcontroller, which is

105 integrated on the PCB, and are powered by a 1800 mAh lithium battery. Protecting the PCB is done with a

106 weather- and waterproof casing, which has been designed (Figure 1-b) with the dimensions 110mm x 38mm

107 x 15mm.

Atmospheric
Measurement
Techniques
Open Access
Discussions

EGU

108 The communication between microcontroller and MEMS sensor on the PCB is either be done by Inter-

109 Integrated Circuit (I2C) or Serial Peripheral Interface (SPI). Both communication methods are bus protocols

110 and allow for serial data transfer. However, SPI handles full-duplex communication, simultaneous communi-

111 cation between microcontroller and MEMS sensor, while I2C is half-duplex. Therefore, I2C has the option of

112 clock stretching, the communication is stopped whenever the MEMS sensor is not able to send data. Besides,

113 I2C has build-in features to verify the data communication (e.g., start/stop bite, acknowledgement of data).

114 Although the I2C protocol is favourable, it requires more power. Furthermore, the microcontroller handles

115 the data storage. The PCB includes a 64 mb flash memory, which is used to store the data. The raw output

116 of the digital MEMS sensors are stored as bits.

2.2 Casing design for pressure measurements

118 The mobile sensor platform is designed to measure atmospheric parameters. Hence, a waterproof casing has

119 been created, by a Formlabs SLA 3D printer [Formlabs, 2020], to protect the PCB. Because of the use of

120 a Durable Resin, the casing is waterproof and air-tight. At the bottom of the casing, a dome structure is

121 integrated (Figure 1-c), which acts as an inlet to both the absolute and differential pressure sensors. Note

122 that the dome is not connected to the inside of the casing. The inlets of both sensors and a capillary are

123 integrated in the dome designs, and sealed with silicon glue, avoiding water and air leakage. Moreover, a

124 Gore-TEX air-vent sticker [Gore-Tex, 2020] is used to cover the dome, which allows airflow but restrains

125 water and salt in case of measurement near or above the ocean.

126 By this design, the volume of the casing acts as a backing volume. One inlet of the differential pressure sensor

127 is attached to the outside (via the dome) while the casing encloses the other inlet. A PEEKsil^{TM} Red series

128 capillary is attached to the outside of the casing, ensuring pressure leakage between the backing volume and

129 the atmosphere.

2.3 GPS

131 For measuring geophysical parameters on a high-resolution temporal scale, it is crucial to know the position

132 and time of the measurement at high precision. To maintain knowledge regarding the position, a GNS2301

133 GPS is mounted on the PCB [Texim Europe, 2013]. The GPS has a spatial accuracy of ± 2.5 m.

134 Besides providing an accurate position, the GPS also prevents drifting of the internal clock of the microcon-

135 troller under the influence of, for example, weather. The time root mean square jitter, the deviation between

136 GPS and true time, is ± 30 nanoseconds.

3 Sensor descriptions

3.1 Infrasound sensor

139 The human audible sound spectrum is approximately between 20 to 20,000 Hz. Frequencies below 20 Hz

140 or above 20 kHz are referred to as infrasound and ultrasound, respectively. The movement of large air

141 volumes generates infrasound signals with amplitudes in the range of millipascals to tens of pascals. Ex-

142 amples of infrasound sources include earthquakes, lightning, meteors, nuclear explosions, interfering oceanic

143 waves and surf [Campus and Christie, 2010]. Detection of infrasound depends on the strength of the signal

144 relative to the noise levels at a remote sensor (array), i.e., the signal-to-noise ratio. The signal strength

145 depends, in turn, on the transmission loss that a signal experiences, while propagating from source to re-

146 ceiver [Waxler and Assink, 2019]. The noise are predominantly determined by local wind noise conditions

147 [Raspet et al., 2019], in addition to the sensor self-noise. Due to the presence of atmospheric waveguides

148 and low absorption at infrasonic frequency [Sutherland and Bass, 2004], infrasonic signals can be detected

149 at long distances from an infrasonic source. Assumed that the source levels are sufficiently high so that the

150 long-range signal is above the ambient noise conditions on the receiver side, and the sensor is sensitive enough

151 to detect the signal.

152 The infrasonic wavefield is conventionally measured with pressure transducers since such scalar measurements

153 are relatively easy to perform. Those measurements can either be performed by absolute or differential

154 pressure sensors. An absolute pressure sensor consists of a sealed aneroid and a measuring cavity, which

155 is connected to the atmosphere. A pressure difference within the measuring cavity will deflect the aneroid

156 capsule. The mechanical deflection is converted to a voltage [Haak and De Wilde, 1996]. The measurement

157 principle of a differential infrasound sensors relies on the deflection of a compliant diaphragm, which is

Atmospheric
Measurement
Techniques
Discussions

158   mounted on a cavity inside the sensor. The membrane deflects due to a pressure difference inside and

159   outside the microphone, which occurs when a sound wave passes. A pressure equalization vent is part of the

160   design to make the microphone insensitive to slowly varying pressure differences originating from long period

161   changes in weather conditions [Ponceau and Bosca, 2010]. Acoustic particle velocity sensors constitute a

162   fundamentally different class of sensors, that measure the airflow over sets of heated wires. This information

163   quantifies the 3-D particle velocity at one location, since the measurement is carried out in three directions

164   [De Bree et al., 2003] [Evers and Haak, 2000]. Although the design of such sensors is more involved and the

165   sensors are far more costly, these sensors do allow for the measurement of sound directivity at one position,

166   besides just the loudness.

167   Various studies show that the sensitivity curves of infrasound sensors [Ponceau and Bosca, 2010] [Merchant, 2015]

168   [Slad and Merchant, 2016] [Marty, 2019] [Nief et al., 2019] lie below the global low ambient noise curves

169   [Brown et al., 2014], which have been generated from global infrasound measurements using the IMS. Typical

170   infrasound sensor networks, such as the IMS, make use of analog sensors that are connected to a separate

171   data logger to convert the measured voltage differences to a digital signal. The characteristic sensitivity of the

172   sensor determines the sensor resolution, i.e., the smallest difference that can be detected by the sensor. The

173   resolution of the built-in analog-to-digital converters (ADC) and the digitizing voltage range determine the

174   resolution of the datalogger. Current state-of-the-art dataloggers have a 24-bit resolution. New infrasound

175   sensor techniques involve digital outputs, since the ADC conversion is realized inside the sensor.

3.1.1   Sensor design

177   In this section, the design of the mobile digital infrasound sensor is discussed, the KNMI mini-microbarometer

178   (mini-MB). The design of this instrument is based on the following requirements. The sensor should have a

179   flat, linear, response over a wide infrasonic frequency band, e.g., 0.05 - 10 Hz. The sensor should be sensitive

180   to the range of pressure perturbations that occur in this frequency band, which are in the range of millipascals

181   to tens of pascals. Moreover, the self-noise of both the sensor and logging components should be below the

182   ambient noise levels of the IMS [Brown et al., 2014]. Taking this into account, the sensor requires as well to

183   be low-cost (i.e., tens of dollars), small in dimensions (i.e., millimeter), and have a low energy consumption

Atmospheric
Measurement
Techniques

Open Access

EGU

Discussions

184   (i.e., milliampere) .

185   In this study, infrasound is measured with a differential pressure sensor. The measurement principle relies

186   on the deflection of a diaphragm, which is mounted between two inlets. One inlet is connected to the

187   atmosphere while the other is connected to a cavity (Figure 2). The digital MEMS DLVR-F50D differential

188   pressure sensor from All Sensors Inc [DLV, 2019] is used as sensing element within the mini-MB. This sensor

189   has a dimension of 16.5mm x 13.0mm x 7.3mm and has a linear response between ± 125 Pa with a maximum

190   error band of ±0.7 Pa. A Wheatstone bridge senses the deflection of the diaphragm by measuring the changes

191   in the piezo-resistive elements attached to the diaphragm. The output of the sensor is an analog voltage,

192   that is subsequently digitized by the built-in 14-bit ADC, offering a maximum resolution of 0.02 Pa/count.

3.1.2   Theoretical response

194   To measure differential pressure, the atmosphere is sampled through inlet A, which has a low resistance

195   (R_1), and is connected to a small fore-volume (V_1). Inlet B is connected to a backing volume (V_2), which is

196   connected to the atmosphere by capillary that acts as a high acoustic resistance (R_2), which determines the

197   low-frequency cut off. Due to an external pressure wave, an observed pressure difference between the two

198   inlets occurs and causes a deflection of the membrane (C_d) (Figure 2-a).

199   A theoretical response, $D(i\omega)$ for a differential pressure sensor, as function of the angular frequency $\omega (= 2\pi f)$,

200   has been derived by [Mentink and Evers, 2011] following [Burridge, 1971]:

$$D(i\omega) = \frac{i\omega\tau_2}{1 + i\omega\tau_2 A + (i\omega)^2 \tau_1 \tau_2 B} \qquad (1)$$

201   where,

$$A = 1 + \frac{\tau_1}{\tau_2} + \frac{R_1}{R_2} + \frac{C_d}{C_2}, \quad B = 1 + C_d(\frac{1}{C_1} + \frac{1}{C_2}) \qquad (2)$$

$$\tau_j = R_j C_j, \quad C_j = \frac{V_j}{P_{\text{atm}}\gamma} \qquad (3)$$

202   and P_{atm} indicates the ambient barometric pressure, and γ is the thermal conduction of air. τ_j represent

203   the time constants, and depend on R_1, and R_2, which are the resistances of the inlet and capillary, and

204   C_1, and C_2, the capacities of the fore and backing volume.

KNMI mini-MB sensor specifications			
Components		**Conditions**	
Inlet length	$l_1 = 3\text{x}10^{-2}\text{m}$	Ambient pressure	$P_{\text{atm}} = 101\text{x}10^3\text{Pa}$
Inlet diameter	$a_1 = 2\text{x}10^{-2}\text{m}$	Isothermal gas constant	$\gamma_{iso} = 1$
Capillary length	$l_2 = 5\text{x}10^{-2}\text{m}$	Adiabatic gas constant	$\gamma_{adi} = 1.403$
Capillary diameter	$a_2 = 1\text{x}10^{-4}\text{m}$	Thermal conductivity	$\kappa = 2.5\text{x}10^{-2} \text{ W m}^{-1}\text{ K}^{-1}$
Diaphragm sensitivity	$C_d = 7.5\text{x}10^{-11}\text{m}^4\text{s}^2\text{kg}^{-1}$	Heat capacity	$\rho\, c_p = 1.1\text{x}10^3 \text{ J m}^{-3}\text{ K}^{-1}$
Parameters			
Inlet resistance	$R_1 = 8.7\text{x}10^3 \text{ kg m}^{-4}\text{ s}^{-1}$	Fore volume	$V_1 = 4.5\text{x}10^{-7} \text{ m}^3$
Capillary resistance	$R_2 = 2.3\text{x}10^{10} \text{ kg m}^{-4}\text{ s}^{-1}$	Backing volume	$V_2 = 16.5\text{x}10^{-6} \text{ m}^3$
Size fore volume	$L_1 = 2\text{x}10^{-4}\text{m}$	Size backing volume	$L_2 = 4\text{x}10^{-4}\text{m}$

Table 1: KNMI mini-MB components, parameter values and standard conditions used in the computations.

205   Figure 2-a represents the sensor setup from an acoustical perspective, where Figure 2-b represents the elec-

206   trical analogs of the sensor. The acoustical pressure difference $(p' = p'_1 - p'_2)$ and volume flux (f') are

207   interpreted as an electrical voltage $(U = U_1 - U_2)$ and current (I). The equivalent of the electrical resistance

208   (R) corresponds to the ratio between acoustical pressure and the volume flux, whereas the capacitance (C)

209   relates to the ratio of volume and ambient barometric pressure. The mechanical sensitivity of the diaphragm

210   (C_d) is the ratio of volume change and pressure change [Zirpel et al., 1978].

211   From an analysis of Eq. 1, it follows that inlet A dominates in the high-frequency limit. Hence, $1/2\pi\tau_1$

212   indicates the high-frequency cut-off of the sensor:

$$\lim_{\omega \to +\infty} D(i\omega) \sim \frac{1}{i\omega\tau_1 B} = \frac{1}{\frac{i\omega R_1 V_1}{P_{\text{atm}}}\left(1 + C_d\left(\frac{P_{\text{atm}}}{V_1} + \frac{P_{\text{atm}}}{V_2}\right)\right)} \tag{4}$$

213   While at low frequencies it is obtained that frequencies much smaller than $1/\tau_2$ are averaged out. Therefore

214   the low-frequency limit can be determined as:

Atmospheric
Measurement
Techniques
Discussions

Open Access

EGU

$$\lim_{\omega \to 0} D(i\omega) \sim i\omega = \frac{i\omega R_2 V_2}{P_{\text{atm}}} \tag{5}$$

215 which is controlled by the characteristics of the capillary, R_2, and the size of the backing volume, V_2. The

216 acoustical resistance of the inlet R_1 and the capillary R_2 is described by using Poiseuille's law [Washburn, 1921],

217 which couples the resistance of airflow through a pipe (i.e., an inlet or capillary) to its length l_j and diameter

218 a_j, by:

$$R_j = \frac{8 l_j \eta}{\pi a_j^4} \tag{6}$$

219 Where η stands for the viscosity of air, which equals 18.27 μPa·s at 18°C. Combining Equations 5 and 6

220 results in the theoretical low-frequency cut-off:

$$f_l \sim \frac{P_{\text{atm}}}{2\pi R_2 V_2} \tag{7}$$

221 Besides the high and low ends of the response, it is of interest to determine the sensor response behavior

222 within the passband ($(\tau_2^{-1} < \omega < \tau_1^{-1})$).

$$D(i\omega) \sim (\tau_2^{-1} < \omega < \tau_1^{-1}) = \frac{1}{1 + \underbrace{\tau_1/\tau_2}_{1} + \underbrace{R_1/R_2}_{2} + \underbrace{C_d/C_2}_{3}} \tag{8}$$

223 The three contributions in the denominator influence the passband behavior of the sensor:

224 1. A broadband frequency response depends on a constant pressure within the reference volume over the

225 frequencies of interest (i.e., $\tau_1 \ll \tau_2$)

226 2. The pressure difference at the diaphragm is determined by the relative acoustical resistances that are

227 connected to the sensor. The stability of the sensor response is assured by the large resistance of the

228 capillary, because of which $R_1 \ll R_2$.

229 3. The sensor response depends on the ratio between the volumetric displacement of the diaphragm (C_d)

230 versus the reference volume (C_2). For the mini-MB, this term can be neglected.

231   Figure 3 shows the theoretical sensor frequency response for amplitude (Fig. 3-a) and phase (Fig. 3-b) for

232   isothermal (red) and adiabatic (blue) behavior. The transitional behavior of the sensor response between

233   isothermal and adiabatic behavior will be discussed in the next section.

234   3.1.3   Adiabatic-Isothermal transition

235   Due to the presence of heat conduction within the sensor, the compressive behavior of air is neither isothermal

236   nor adiabatic. Instead, a transition from isothermal to adiabatic behavior is expected in the infrasonic

237   frequency band [Richiardone, 1993] [Mentink and Evers, 2011]. In the transition zone, the heat capacity

238   ratio can be effectively described by:

$$\overline{\gamma} = \Lambda \gamma \tag{9}$$

239   where Λ indicates the correction factor, to heat capacity ratio γ. A difference in Λ will influence the capaci-

240   tance values of the fore and backing volumes (Eq. 3).

241   Whether a sound wave in an enclusure behaves isothermally or adiabatically depends on the size of the

242   thermal penetration depth δ_t relative to characteristic length L of the enclosure. L is defined as the ratio

243   between the volume and surface of the enclosure, i.e. $L = \frac{V}{S}$. The thermal penetration depth is specified as

244   the gas layer thickness in which heat can diffuse through, during the time of one wave period and is derived

245   as $\delta_t = \sqrt{\frac{2\alpha}{\omega}}$. Where $\alpha = \frac{\kappa}{\rho c_p}$ indicates the thermal diffusivity, defined as ratio of thermal conductivity (κ)

246   and heat capacity per unit volume (ρc_p). Adiabatic gas behaviour is obtained when $\frac{\delta_t}{L} \ll 1$, isothermal gas

247   behaviour when $\frac{\delta_t}{L} \gg 1$. The correction factor Λ is a function of δ_t/L, and is thus frequency dependent,

248   which can be derived as:

$$|\Lambda| = \sqrt{X^2 + Y^2}, \quad \arg(\Lambda) = \frac{\pi}{2} + \arctan(\frac{X}{Y}) \tag{10}$$

249   where

$$X = x(\gamma_{adi} - 1) - \gamma_{adi}, \quad Y = y(\gamma_{adi} - 1) \tag{11}$$

Atmospheric
Measurement
Techniques
Discussions

---

250   x and y represent the real and imaginary components of a complex-valued function $Z(\frac{\delta_t}{L})$, which is dependent

251   on the geometrical shape of the enclosure and the thermal pentration depth. In between the adiabatic and

252   isothermal limits, the correction factor Λ describes the transition from an adiabatic heat ratio (i.e., $\gamma = 1.4$)

253   to an isothermal heat ratio, i.e. $\gamma = 1$. The transition frequency $\bar{f}$ defines the point where the maximum

254   correction of Λ occurs, i.e., for which $L\delta_t \approx 1$, from which follows that $\bar{f} = \frac{\alpha}{\pi L^2}$.

255   In case of the mini-MB the fore and backing volume have different shapes and sizes. The backing volume can

256   be described as a long cylinder, L_2, whereas the fore volume has the shape of a rectangular, L_1. According to

257   those geometries, the transition frequency $\overline{f}$ of the fore and backing volume are 0.5 and 2.2 Hz, respectively.

258   Since $\overline{f}_1 \cdot \tau_1 \ll 1$ and $\overline{f}_2 \cdot \tau_2 \gg 1$ the sensor response above τ_1^{-1} is adiabatic, while the response below τ_2^{-1}

259   is isothermal. Therefore the main effect of the thermal conduction correction is found to be in the passband

260   region (Eq. 8).

261   The mini-MB has been designed to have a broadband response, therefore only the third term of the dominator

262   is influenced by the correction factor. The effect of thermal conduction to the response is due to ratio $\frac{C_d}{C_2}$,

263   which means that the correction factor is characterized by the geometric component of the backing volume.

$$Z(\frac{\delta_t}{L}) = 1 - \frac{2J_1(\zeta)}{\zeta J_0(\zeta)} \tag{12}$$

264   here Z indicates the characteristic correction assuming a long cylinder [Mentink and Evers, 2011]. $\zeta =$

265   $\sqrt{-2i}\frac{L}{\delta_t}$ indicates the ratio of L to δ_t, while J_0 and J_1 are zeroth and first order Bessel functions of the first

266   kind.

267   The corrected theoretical sensor response is obtained by substituting $\overline{C_j} = \frac{C_j}{\Lambda}$. Figure 3-c shows the value of

268   $\overline{\gamma}$ in the transaction zone between isothermal and adiabatic gas behaviour. The black line in Figure 3-a and

269   b indicates the corrected theoretical sensor response.

270   In the case of the mini-MB the isothermal-to-adiabatic transition results in an effect on the amplitude of

271   $\Delta|D| = (\gamma - 1)\frac{C_d}{C_2} = 2.8\%$ and on the phase of less than a degree. Note that $\frac{C_d}{C_2} \ll 1$ implies that the

272   backing volume is relatively large such that the change in gas behavior does not influence the sensitivity of

273   the diaphragm.

3.1.4 Gore-Tex air-vent

As discussed in Section 3.1.2., the high and low-frequency cut-off are controlled by the resistivity of the inlet and backing volume, respectively. A Gore-Tex V9 sticker is added to the opening of the pressure dome of the casing, which changes the resistivity of the inlets. The Gore-Tex V9 vent allows an airflow of $2 \times 10^{-8} \mathrm{m}^3\mathrm{s}^{-1}\mathrm{m}^{-2}$. Poiseuille's second law, Equation 6, shows the airflow resistivity caused by an open pipe, and can be re-written as;

$$R_j = \frac{\Delta p}{q_v} \tag{13}$$

where Δp indicates the pressure difference between both sides of the pipe, and q_v the volumetric airflow.

For the differential pressures that the mini-MB sensor is able to sense, ranging from 0.02 to 125 Pa, with a Gore-Tex air-vent area of 5×10^{-2} m^2, the equivalent resistivity R_{gore} is ranging from 5×10^5 to $3.125 \times 10^8 \mathrm{kgm}^{-4}\mathrm{s}^{-1}$. Comparing the resistivity of the air-vent with the resistivity values of the capillary and the sensors inlet, Table 1, it follows that only the resistivity of the inlet will be influenced by the air-vent. Assuming the vent behaves linear, the high frequency cut-off of the sensor decreases to a value of around 15 Hz. Figure 3 shows the theoretical transfer function for the mini-MB with a Gore-Tex air-vent attached to the inlet. The high frequency cut-off is shifting between the dotted line and the dashed line, due to varying values of R_{gore}.

3.1.5 Experimental response

The theoretical sensor response describes the high and low-frequency cut-off. From Eq. 7 and the parameters listed in Table 1, it follows that the mini-MB has a theoretical low-frequency cut-off of 0.042Hz. A sudden over or under pressure (i.e., impulse response) is applied to the sensor to determine the low-frequency cut-off experimentally[Evers and Haak, 2000]. The impulse forces the diaphragm out of equilibrium. The capillary and the size of the backing volume control the time to return into equilibrium again. The time it takes for the diaphragm to reach equilibrium again corresponds to a characteristic relaxation time that is proportional to the low-frequency cut-off.

297 The outcome of the experimental low-frequency cut-off was determined to be 0.044±0.0025Hz. The theoretical

298 low frequency cut-off falls within the error margins of the experimental cut-off frequency. Small difference

299 between both are assumed to be due to experimental errors in timing the relaxation time as well as small

300 imperfections in the used capillary [Evers, 2008]. It follows from Eq. 6 that the low-frequency cut-off is

301 inversely proportional to the radius to the fourth power. Hence, a one percent deviation in the capillary

302 radius will lead to a four percent deviation in low-frequency cut-off.

303 ### 3.1.6 Sensor self-noise

304 The resolution, the smallest change detectable by a sensor, depends on the sensor measurement range and

305 the number of ADC bits. Having a linear response over a pressure range of $\pm$ 125 Pa and a 14-bit build-in

306 ADC results in a resolution of 0.02 Pa/count. The accuracy of the measurement depends, besides the ADC

307 resolution, on the internal error of the sensor, the self-noise. The self-noise corresponds to the deformation of

308 the diaphragm caused by the mass of the diaphragm plus the electrical noise from the digitiser. As it is a dig-

309 ital sensor, it is not possible to follow the conventional methods to determine self-noise [Sleeman et al., 2006].

310 Therefore the self-noise is determined by opening both inlets to a closed pressure chamber, ensuring no pres-

311 sure difference between both inlets. The outcome stated that the self-noise falls within the maximum error

312 band of the sensor, $\pm$0.7 Pa [DLV, 2019]. Since no backing volume is used, and the cavities at both sides of

313 the diaphragm are small, the relation $\frac{C_d}{C_2}$ changes (Eq. 8). Due to this, it is necessary to correct the sensor

314 response for the adiabatic to isothermal transition. (Section 3.1.3).

315 The consistency of the self-noise is determined by calculating the Power Spectral Density (PSD) curves for

316 each hour over a test period of 24 hours [Merchant and Hart, 2011]. Figure 4-a shows in black the average

317 90 percentile confidence interval of the self-noise. Note that the instrumental self-noise exceeds the global

318 low noise model [Brown et al., 2014] at frequencies above 0.4 Hz. Compared to high-fidelity equipment

319 that typically fall completely below the global low noise models, such self-noise levels are relatively high,

320 yet comparable to levels that are attained by similar sensor designs [Marcillo et al., 2012]. Furthermore,

321 note that the self-noise follows the dynamic range of a 12-bit ADC, as indicated by the gray dotted line

322 [Sleeman et al., 2006]. The sensor has a maximum 'no missing code' of 12-bits, the effective number of bits

Atmospheric
Measurement
Techniques
Discussions

Open Access
EGU

323 [DLV, 2019].

3.1.7 Sensor comparison

325 A comparison between the mini-MB and a Hyperion IFS-5111 sensor [Merchant, 2015] is made to assess the

326 performance of the mini-MB relative to the reference Hyperion sensor. Both sensors have been placed inside

327 a cabin next to the outside sensor test facility at the leading author's institute. There is a connection to the

328 outside pressure field through air holes in the wall of the cabin. The Hyperion sensor has been configured

329 with a high-frequency (HF) shroud. Figure 4-a and b show the PDF [Merchant and Hart, 2011] of the data

330 recorded by the mini-MB and the Hyperion sensor, respectively. Both sensors resolved the characteristic

331 microbarom peak around 0.2Hz [Christie and Campus, 2010].

332 A direct comparison of the pressure recordings is shown in Figures 4-c, -d, and -e. Figure 4-c shows the

333 absolute difference in amplitude over frequency, where panel d indicates the phase difference between both

334 sensors. Panel e shows the relative difference between the mini-MB and the Hyperion sensor. The sensors are

335 in good agreement over the passband frequencies. A larger deviation is shown for the low end ($f < 0.07$ Hz)

336 and high end frequencies($f > 8$ Hz). At frequencies between 0.07 and 1 Hz, the pressure values are positively

337 biased by 5 ± 1 dB, which equals an error of $\pm$ 0.005 Pa (Figure 4-e). Above 1 Hz, the pressure values are

338 biased by 10 ± 5 dB, which equals an error of $\pm$ 0.02 Pa.

339 The deviation in the low frequency spectrum is caused by the backing volume. The high frequency deviation

340 is due to the relatively high noise level of the mini-MB. For the higher frequencies, the mini-MB PDF follows

341 the 12-bit dynamic range. Only in case of significant events or loud ambient noise, the sensor is capable of

342 sensing pressure perturbations in the high-frequency range. Nonetheless, over the entire frequency band the

343 mini-MB falls within a 30 dB error range compared to the Hyperion IFS-5111 sensor.

3.2 Meteorological parameters

345 The detectability of infrasound is directly linked to wind noise conditions and the stability of the atmosphere

346 in the surrounding of the infrasound sensor, since noise levels are increased when turbulence levels are high.

347 Therefore, it is beneficial to have simultaneous measurements of the basic meteorological parameters, i.e.,

348 pressure, wind and temperature. The sub-sections below describe the different meteorological measurements

349 contained on the sensor platform.

3.2.1 Barometric pressure sensor

351 The barometric pressure is sensed by the LPS33HW sensor [STMicroelectronics, 2017], which is part of the

352 pressure dome. Similarly to the differential pressure sensor, piezo-resistive crystals measure the barometric

353 pressure.

354 Calibration tests are performed within a pressure chamber, in which a cycle of static pressures between 960

355 and 1070 hPa can be produced. Besides the MEMS sensor, the chamber is equipped with a reference sensor.

356 This procedure resulted in a calibration curve, which describes the pressure dependent systematic bias. After

357 correcting for the bias, the LPS sensor has an accuracy of ± 0.1 hPa, i.e., the LPS sensors measures values

358 that are within ± 0.1 hPa of the value measured by the KNMI reference sensor. Furthermore, the LPS sensor

359 has been field tested, along a Paroscientific Digiquartz 1015A barometer, which has an accuracy of 0.05 hPa.

360 From the distribution of observations, it can be estimated that the LPS sensor has a precision of ±0.1 hPa

361 for 93% of the time. For the remainder, the maximum deviation was ±0.15 hPa.

3.2.2 Wind sensor

363 The pressure field at infrasonic frequencies consists, in addition to coherent acoustic signals, to a large

364 degree of pressure perturbations due to wind and turbulence, and which is generally referred to as wind-noise

365 [Walker and Hedlin, 2010]. Wind noise is present over the complete infrasonic frequency range with a typical

366 noise amplitude level decrease with increasing frequencies, following a $f^{-5/3}$ slope [Raspet et al., 2019].

367 For the reduction of wind noise a Wind-Noise-Reduction-System (WNRS) can be put in place [Walker and Hedlin, 2010]

368 [Raspet et al., 2019]. Most WNRSs applied consist of a non-porous pipe rosette, with low impedance inlets

369 at the end of each pipe. All pipes are connected to four main pipes, which connect to the microbarometer.

370 Doing so, the atmosphere is sampled over a larger area, and thus small incoherent pressure perturbations

371 (e.g., wind) are filtered out.

372 The sensor presented in this paper is designed for mobile sampling campaigns. In such cases, the application

16

₃₇₃ of similar WNRS filters cannot be attained. Not having a WNRS decreases the SNR, measuring wind with

₃₇₄ an anemometer will give an insight into the wind conditions. Therefore, a simultaneous measurement of wind

₃₇₅ and infrasound provides better insight into the infrasonic SNR conditions.

Sensor design

₃₇₇ To measure the wind conditions, a 2D omni-directional heat mass flow sensor has been designed, which is a

₃₇₈ robust and passive anemometer (Figure 6-a). The sensor is built with a central heating element, which heats

₃₇₉ up to approximately 80°C, and is circularly surrounded by six TDK thermistors [TDK, 2018]. Depending on

₃₈₀ the wind direction and speed, the temperature field around the center element is modified. The wind speed

₃₈₁ and direction can be estimated from the 2D temperature gradient, i.e., its absolute value and direction.

Theoretical response

₃₈₃ The six sensing elements are placed within a distance of one centimeter from the heating element, while two

₃₈₄ thermistors and the heating element are at a spatial angle of 60°. The thermistors are used to measure the

₃₈₅ temperature gradient that is caused by the wind flow, since the resistance is strongly sensitive to temperature.

₃₈₆ The thermistors are made of semiconductor material and have a negative temperature coefficient. The

₃₈₇ resistance decreases non-linearly with increasing temperature. The Steinhart-Hart equation approximately

₃₈₈ describes the temperature T as a function of resistance value R_Ω [Steinhart and Hart, 1968]:

$$\frac{1}{T} = C_{\Omega_1} + C_{\Omega_2}(\ln(R_\Omega)) + C_{\Omega_3}(\ln(R_\Omega)^3) \tag{14}$$

₃₈₉ where $C_{\Omega_1}, C_{\Omega_2}$, and C_{Ω_3} are the thermistor constants, which can be determined by taking three calibration

₃₉₀ measurements, for which the temperature and resistance are known, and solving the three equations simulta-

₃₉₁ neously. Figure 6-b shows the sensitivity curve for the TDK thermistor. The thermistor has a relative value

₃₉₂ of 1Ω at $25°C$, and a precision of $\pm4\%/°C$, which leads to a 0.05°C error. In the next section, this error

₃₉₃ value is placed in context by modeling the expected temperate difference under representative meteorological

₃₉₄ conditions.

Numerical sensor response

The heating element needs to be able to transfer a minimum temperature difference around the sensing

elements (i.e., the sensing elements error). A numerical model has been built in ANSYS to define the amount

of temperature difference around the sensing elements under different meteorological circumstances. The

model is a first approximation of the sensitivity and is based on homogeneous laminar airflow passing by the

sensor. Turbulent flow along the anemometer causes uncertainties in wind direction and speed.

This approach follows a numerical forward modeling technique to approximate the shape of the heat probe

and its intensity at a sensing element. The model was run at stable meteorological parameters (i.e., 8°C air

temperature, 50% humidity, and 10 m/s wind speed). The outcome shows that under those circumstances,

the sensing element experiences a temperature difference of around 4°C. Together with the outcome of the

sensitivity curve of the thermistors, it is concluded that the designed sensor can resolve this airflow and is

used to estimate wind speed and direction.

Reference calibration

Experimental calibration of the anemometer has been performed at the KNMI's calibration lab. The cali-

bration lab features a wind tunnel, which generates a laminar airflow ranging between 0 - 20 m/s. Within

the wind-tunnel, two mechanical anemometers are installed, which serve as reference sensors. The mobile

platform with its MEMS anemometer is installed right below one of the reference sensors to ensure that the

mobile platform does not obstruct the laminar flow in the tunnel.

The calibration procedure consists of multiple independent calibration tests that will be described next. First,

the sensor is placed inside the wind tunnel while there is no airflow. This way, the relative difference between

the sensing elements is determined, the so-called zero-measurement. By correcting for the relative difference,

the sensor is corrected for the internal bias, which varies around $\pm$ 25 ohm. After correcting for the sensor

bias, the sensor is placed at different angles with respect to the air flow. For every angle, the flow speed is

varied between 0 tot 20 m/s.

The calibration shows that the measured resistance of the thermistors increases with increasing wind speeds.

420 High wind speeds increasingly cool down the thermistors, resulting in higher resistances. Figure 6-c shows

421 the measured resistance of the six thermistors over the wind speed. To convert resistance into wind speed, a

422 polynomial curve has been fitted over the average measured resistance (Fig. 6-c, black line).

423 The accuracy of the wind direction is determined by interpolating the measured velocities into a gradient

424 field over the sensor. The wind direction is obtained by calculating the mean gradient vector of this gradient

425 field. Three different sensor set-ups show the accuracy and precision over increasing wind speeds as a function

426 of directivity. The outcome of calibration set-ups 1 (270°), 2 (90°), and 3 (60°) are shown respectively in

427 Figure 6-d, -e, and -f. The mean direction over all wind speeds, for the three set-ups, are 93°, 265°, and 62°.

428 The standard deviation shows that the accuracy of the sensor is ±18°. Furthermore, it is shown that the

429 precision of the wind direction increases with increasing wind speeds.

3.3   Accelerometer

431 The sensing element of the infrasound sensor on this platform is a sensitive diaphragm. Strong accelerations

432 of the platform will cause a deflection of the diaphragm and may obscure infrasonic signal levels. In addition,

433 such accelerations may be interpreted erroneously as infrasound if no independent accelerometer information

434 is available. To be able to separate the mechanical response of the sensor from actual signals of interest, the

435 platform measures accelerations for which the LSM303, a 6-axis inertial measurement unit (IMU), is deployed

436 [STMicroelectronics, 2018]. The LSM303 consists of a 3-axis accelerometer and 3-axis magnetometer. The

437 measurement range of the accelerometer varies between approximately 2-16 g. The magnetometer is out of

438 the scope of this study, and therefore neglected for the remainder.

439 Accelerometers measure differential movement between the gravitational field vector and its reference frame.

440 In the absence of linear acceleration, the sensor measures the rotated gravitational field vector, which can be

441 used to calibrate the sensor. A rotational movement of the sensor will result in an acceleration. The IMU

442 is a digital sensor with a built-in 16-bits ADC and has a resolution of 0.06 mg when choosing the lowest

443 measurement range.

444 A comparison test has been carried out in the seismic pavilion of the author's institute. Inside this pavilion

445 the LSM is compared to a Streckeisen STS-2 seismometer connected to a Quanterra Q330, as a reference

Atmospheric
Measurement
Techniques
Discussions

Open Access

EGU

446 sensor [KNMI, 1993]. Both sensors are installed on pillars, to ensure a good coupling between the subsurface

447 and the sensor. The comparison test, which is based on 24 hours of recording, shows that the accuracy of

448 the LSM303 3-axis accelerometer is ±1.5 mg (1.5 cm/s^2). Figure 7 shows the PDF's of the comparison test

449 for the MEMS and STS-2 sensor. While the sensors are deployed on the same seismic pillar, and are thus

450 subject to similar seismic noise conditions, the MEMS sensor was not able to measure ambient seismic noise

451 ([Peterson, 1993] [McNamara and Buland, 2004]) due to its high self-noise level. The LSM accelerometer

452 exceeds both the U.S. Geological Survey New High Noise Model (NHNM) [Peterson, 1993] as well as the

453 STS-2 reference sensor by at least 35 dB.

454 It is therefore unlikely to use this IMU for monitoring purposes of ambient seismic noise or teleseismic events.

455 Previous studies drew similar conclusions concerning the performance of MEMS accelerometers. Various

456 calibration set-ups are considered while comparing MEMS accelerometers with conventional accelerometers

457 of geophones [Hons et al., 2008] [Albarbar et al., 2009] [Anthony et al., 2019], each concluding that the ac-

458 curacy of the MEMS is not sufficient for recording ambient seismic noise. However, strong local events or in

459 case of extremely noisy environments the MEMS sensor will be able to resolve those seismic signals.

460 4 Discussion and Conclusion

461 In this study, the constructional efforts and calibration protocols of the "infrasound-logger" are presented.

462 The "infrasound-logger" is a low-cost mobile multidisciplinary sensor platform for the monitoring of geophys-

463 ical quantities and includes sensors for the measurement of infrasound, acceleration, as well as barometric

464 pressure and wind.

465 The platform uses the newest sensor technology, i.e., digital MEMS, which have a build-in ADC. The MSP430

466 programable microcontroller unit controls the sampling of the ADC and the storage of the data samples. A

467 MEMS GPS is unit to determine positioning and to prevent clock-drift. Due to the small dimension of MEMS,

468 and their low energy consumption, the "infrasound-logger" is a pocket-size measurement platform, powered

469 by an 1800 mAh lithium battery. The platform does not require any infrastructure (e.g., data connection,

470 power supply and specific mounting) like commonly used for the deployment of high-fidelity systems, which

471 makes it mobile and allows rapid deployments as well as measurements at remote places.

472 The "infrasound-logger" is specifically designed to measure infrasound. The platform hosts the KNMI mini-

473 MB, which is a novel design with a pressure dome as inlet, the casing as backing-volume with a PEEKsil

474 capillary, and the DLVR-F50D as sensing element. The low-frequency cut-off of mini-MB depends on the

475 size of the backing volume, and the characteristics of the capillary. The high-frequency cut-off depends on

476 the inlet parameters of the mini-MB, which is partly controlled by a Gore-Tex air-vent (Section 3.1.4). The

477 "infrasound-logger" has a low-frequency cut-off frequency of 0.044 ± 0.0025 Hz, while the high-frequency

478 cut-off varies between 15 and 90 Hz.

479 A comparison between the mini-MB and a Hyperion infrasound sensor [Merchant, 2015] has shown the differ-

480 ences in amplitude and phase (Figure 4. For the passband frequencies band the mini-MB has an amplitude

481 difference of 30 dB compared to the Hyperion sensor. For the lower frequencies the sensors are in good agree-

482 ment, both sensors resolved the characteristic microbarom peak around 0.2 Hz [Christie and Campus, 2010].

483 The higher frequencies, however, show small deviations, which is due to the relatively high noise band of

484 the mini-MB. From 8 Hz onward, the PDF of the mini-MB follows the 12-bit dynamic range of the ADC.

485 Nonetheless, the mini-MB is able to resolve infrasonic ambient noise field up to $\pm$ 8 Hz. Only in case of

486 significant events or extremely noisy conditions, the sensor is capable of sensing pressure perturbations in

487 the higher frequency range.

488 When the wind noise levels are high, infrasound signals can be masked and remain undetected. Therefore, the

489 sensor platform presents a robust passive anemometer to give insights in the wind conditions during infrasonic

490 measurements. The MEMS anemometer is built up as an omnidirectional sensor. Numerical tests indicate

491 that the temperature difference caused by a wind flow around the thermistors should be significant to be

492 sensed. For validation, the anemometer has been calibrated inside a wind tunnel. Figure 6 shows the outcome

493 of the calibration tests. Based on this outcome, one can conclude that the anemometer can determine wind

494 direction and wind speed, given that the sensor is calibrated. The sensor measures a difference in resistance,

495 which is relative compared to wind speed and direction. Although the sensor is resolving wind direction

496 and speed, the resolution is poor compared to the reference sensors. For the estimation of a 2D gradient

497 (assuming the gradient is uniform), in principle only four degrees of freedom are needed: 2 in the x-direction,

Atmospheric
Measurement
Techniques
Discussions

Open Access
EGU

498 2 in the y-direction. Therefore, the proposed system should be over determined in this case. Nonetheless,

499 the resolution outcome of the MEMS anemometer shows opposite. It is likely that the temperature gradient

500 is not strong enough to provide a wind direction resolution higher as $30°$. A slight deviation is z position (a

501 height difference) between the thermistors can cause such a reduction of temperature gradient.

502 Besides an anemometer and infrasound sensor, the platform also hosts a barometric pressure sensor, an

503 accelerometer, and GPS. Each sensor has been calibrated and compared with a reference sensor. It was

504 shown that the accelerometer has a relatively high self-noise, which restricts the sensors ability to determine

505 the ambient seismic noise [Peterson, 1993] [McNamara and Buland, 2004]. Nonetheless, the sensor will most

506 likely resolve local transient events, which influences the sensitivity of the mini-MB and its ability to resolve

507 infrasonic sources. The barometric sensor shows good agreement with a reference sensor (Figure 5). Absolute

508 pressure perturbations due to the weather are resolved. After calibration, the sensor has a precision of ± 0.1

509 hPa for 93% of the time. For the remainder maximum deviation, compared to the reference sensor, was

510 ± 0.15 hPa.

511 Calibration tests, performed in this study and previous literature, show that the MEMS sensors perform

512 less than the commonly used high-fidelity sensors. The self-noise of the sensors is a critical problem.

513 Furthermore, the manufacturer of the MEMS sensors highlight there is a significant change of measure-

514 ment drift [DLV, 2019] [TDK, 2018] [STMicroelectronics, 2017] [STMicroelectronics, 2018], regular calibra-

515 tion is needed. Nonetheless, the MEMS sensor techniques are continuously developing [Jacob et al., 2014]

516 [Johari, 2003]. The design of the "infrasound-logger" is such that the platform can be adjust and improved

517 by adding or swapping sensors. Mobile sensor platforms, build up by PCB's and digital MEMS sensors, are

518 therefor scalable, flexible, and ready for various geophysical measurements.

519 Nonetheless, a low-cost mobile multidisciplinary sensor platform can complement existing high-fidelity geo-

520 physical sensor networks. This study showed that, as long as the MEMS are well-calibrated, they perform

521 in agreement with the reference sensors. Therefore, the 'infrasound-logger' can contribute significantly to

522 providing observations during rapid deployments, to complement the existing sensor network by increasing

523 the number of observations. Although the sensor data does not fully satisfy the measurement requirements,

524 the improve of spatial resolution enables stacking the observations. This can be realized by stacking the

Atmospheric
Measurement
Techniques
Discussions

output of various sensor platforms, or by adding more sensors to the same sensor platform and averaging the output [Nishimura et al., 2019]. Stacking improves the signal-to-noise ratio increases by $1/\sqrt{N}$, where N is the number of observations. Furthermore, the platform enables measurement campaigns at remote places (e.g., weather towers, weather balloons).

Acknowledgements

References

[DLV, 2019] (2019). Technical Report DLVR Series Low Voltage Digital Pressure Sensors. `https://www.allsensors.com/datasheets/DS-0300_Rev_E.pdf`.

[Albarbar et al., 2009] Albarbar, A., Badri, A., Sinha, J. K., and Starr, A. (2009). Performance evaluation of mems accelerometers. *Measurement*, 42(5):790–795.

[Anderson et al., 2018] Anderson, J. F., Johnson, J. B., Bowman, D. C., and Ronan, T. J. (2018). The gem infrasound logger and custom-built instrumentation. *Seismological Research Letters*, 89(1):153–164.

[Anthony et al., 2019] Anthony, R. E., Ringler, A. T., Wilson, D. C., and Wolin, E. (2019). Do low-cost seismographs perform well enough for your network? an overview of laboratory tests and field observations of the osop raspberry shake 4d. *Seismological Research Letters*, 90(1):219–228.

547 [Assink et al., 2018] Assink, J., Averbuch, G., Shani-Kadmiel, S., Smets, P., and Evers, L. (2018). A seismo-

548   acoustic analysis of the 2017 north korean nuclear test. *Seismological Research Letters*, 89(6):2025–2033.

549 [Averbuch et al., 2020] Averbuch, G., Assink, J. D., and Evers, L. G. (2020). Long-range atmospheric infra-

550   sound propagation from subsurface sources. *The Journal of the Acoustical Society of America*, 147(2):1264–

551   1274.

552 [Blanc et al., 2018] Blanc, E., Ceranna, L., Hauchecorne, A., Charlton-Perez, A., Marchetti, E., Evers, L. G.,

553   Kvaerna, T., Lastovicka, J., Eliasson, L., Crosby, N. B., et al. (2018). Toward an improved representation

554   of middle atmospheric dynamics thanks to the arise project. *Surveys in geophysics*, 39(2):171–225.

555 [Brown et al., 2014] Brown, D., Ceranna, L., Prior, M., Mialle, P., and Le Bras, R. J. (2014). The idc

556   seismic, hydroacoustic and infrasound global low and high noise models. *Pure and Applied Geophysics*,

557   171(3-5):361–375.

558 [Burridge, 1971] Burridge, R. (1971). The acoustics of pipe arrays. *Geophysical Journal International*, 26(1-

559   4):53–69.

560 [Campus and Christie, 2010] Campus, P. and Christie, D. (2010). Worldwide observations of infrasonic

561   waves. In *Infrasound monitoring for atmospheric studies*, pages 185–234. Springer.

562 [Christie and Campus, 2010] Christie, D. and Campus, P. (2010). The ims infrasound network: Design

563   and establishment of infrasound stations. In *Infrasound monitoring for atmospheric studies*, pages 29–75.

564   Springer.

565 [Cornes et al., 2020] Cornes, R. C., Dirksen, M., and Sluiter, R. (2020). Correcting citizen-science air tem-

566   perature measurements across the netherlands for short wave radiation bias. *Meteorological Applications*,

567   27(1):e1814.

568 [D'Alessandro et al., 2014] D'Alessandro, A., Luzio, D., and D'Anna, G. (2014). Urban mems based seismic

569   network for post-earthquakes rapid disaster assessment. *Advances in Geosciences*.

570 [De Bree et al., 2003] De Bree, H.-E. et al. (2003). The microflown: An acoustic particle velocity sensor.

571   *Acoustics Australia*, 31(3):91–94.

[Evers, 2008] Evers, L. G. (2008). *The inaudible symphony: on the detection and source identification of atmospheric infrasound.* PhD thesis, TU Delft, Delft University of Technology.

[Evers and Haak, 2000] Evers, L. G. and Haak, H. W. (2000). *The Deelen Infrasound Array: on the detection and identification of infrasound.* Koninklijk Nederlands Meteorologisch Instituut.

[Fang et al., 2010] Fang, Z., Zhao, Z., Du, L., Zhang, J., Pang, C., and Geng, D. (2010). A new portable micro weather station. In *2010 IEEE 5th International Conference on Nano/Micro Engineered and Molecular Systems*, pages 379–382. IEEE.

[Formlabs, 2020] Formlabs (2020). *Technical Report Formlabs 3D printer.* Formlabs.

[Garcia-Marti et al., 2019] Garcia-Marti, I., de Haij, M., Noteboom, J. W., van der Schrier, G., and de Valk, C. (2019). Using volunteered weather observations to explore urban and regional weather patterns in the netherlands. *AGUFM*, 2019:IN22A–08.

[Gore-Tex, 2020] Gore-Tex (2020). *Technical Report Gore TEX air vents.* Gore-Tex.

[Grangeon and Lesage, 2019] Grangeon, J. and Lesage, P. (2019). A robust, low-cost and well-calibrated infrasound sensor for volcano monitoring. *Journal of Volcanology and Geothermal Research*, 387:106668.

[Green et al., 2012] Green, D., Matoza, R., Vergoz, J., and Le Pichon, A. (2012). Infrasonic propagation from the 2010 eyjafjallajökull eruption: Investigating the influence of stratospheric solar tides. *Journal of Geophysical Research: Atmospheres*, 117(D21).

[Haak and De Wilde, 1996] Haak, H. W. and De Wilde, G. (1996). *Microbarograph systems for the infrasonic detection of nuclear explosions.* Royal Netherlands Meteorological Institute, Seismology Division.

[Homeijer et al., 2011] Homeijer, B., Lazaroff, D., Milligan, D., Alley, R., Wu, J., Szepesi, M., Bicknell, B., Zhang, Z., Walmsley, R., and Hartwell, P. (2011). Hewlett packard's seismic grade mems accelerometer. In *2011 IEEE 24th International Conference on Micro Electro Mechanical Systems*, pages 585–588. IEEE.

[Homeijer et al., 2014] Homeijer, B. D., Milligan, D. J., and Hutt, C. R. (2014). A brief test of the hewlett-packard mems seismic accelerometer. *US Geological Survey Open-file Report*, (2014-1047).

596   [Hons et al., 2008] Hons, M., Stewart, R., Lawton, D., Bertram, M., and Hauer, G. (2008). Field data

597   comparisons of mems accelerometers and analog geophones. *The Leading Edge*, 27(7):896–903.

598   [Huang et al., 2003] Huang, Q.-A., Qin, M., Zhang, Z., Zhou, M., Gu, L., Zhu, H., Hu, D., Hu, Z., Xu, G.,

599   and Liu, Z. (2003). Weather station on a chip. In *SENSORS, 2003 IEEE*, volume 2, pages 1106–1113.

600   IEEE.

601   [Jacob et al., 2014] Jacob, R. T., Manjiyani, Z. A. A., et al. (2014). Development of mems based 3-axis

602   accelerometer for hand movement monitoring. *International Journal of Computer Science and Engineering

603   Communications*, 2(1):87–92.

604   [Johari, 2003] Johari, H. (2003). Development of mems sensors for measurements of pressure, relative hu-

605   midity, and temperature.

606   [KNMI, 1993] KNMI (1993). Netherlands Seismic and Acoustic Network. Royal Netherlands Meteorological

607   Institute (KNMI), Other/Seismic Network. 10.21944/e970fd34-23b9-3411-b366-e4f72877d2c5.

608   [Laine and Mougenot, 2007] Laine, J. and Mougenot, D. (2007). Benefits of mems based seismic accelerom-

609   eters for oil exploration. In *TRANSDUCERS 2007-2007 International Solid-State Sensors, Actuators and

610   Microsystems Conference*, pages 1473–1477. IEEE.

611   [Ma et al., 2011] Ma, R.-H., Wang, Y.-H., and Lee, C.-Y. (2011). Wireless remote weather monitoring system

612   based on mems technologies. *Sensors*, 11(3):2715–2727.

613   [Marcillo et al., 2012] Marcillo, O., Johnson, J. B., and Hart, D. (2012). Implementation, characterization,

614   and evaluation of an inexpensive low-power low-noise infrasound sensor based on a micromachined dif-

615   ferential pressure transducer and a mechanical filter. *Journal of Atmospheric and Oceanic Technology*,

616   29(9):1275–1284.

617   [Marty, 2019] Marty, J. (2019). The ims infrasound network: current status and technological developments.

618   In *Infrasound Monitoring for Atmospheric Studies*, pages 3–62. Springer.

619   [McNamara and Buland, 2004] McNamara, D. E. and Buland, R. P. (2004). Ambient noise levels in the

620   continental united states. *Bulletin of the seismological society of America*, 94(4):1517–1527.

Atmospheric
Measurement
Techniques
Discussions

---

621 [Mentink and Evers, 2011] Mentink, J. H. and Evers, L. G. (2011). Frequency response and design parameters

622   for differential microbarometers. *The Journal of the Acoustical Society of America*, 130(1):33–41.

623 [Merchant, 2015] Merchant, B. J. (2015). Hyperion 5113/gp infrasound sensor evaluation. *Sandia Report*

624   *SAND2015–7075, Sandia National Laboratories*.

625 [Merchant and Hart, 2011] Merchant, B. J. and Hart, D. M. (2011). Component evaluation testing and

626   analysis algorithms. *Sandia National Laboratories Technical Report No. SAND2011-8265*.

627 [Milligan et al., 2011] Milligan, D. J., Homeijer, B. D., and Walmsley, R. G. (2011). An ultra-low noise mems

628   accelerometer for seismic imaging. In *SENSORS, 2011 IEEE*, pages 1281–1284. IEEE.

629 [Nief et al., 2019] Nief, G., Talmadge, C., Rothman, J., and Gabrielson, T. (2019). New generations of

630   infrasound sensors: technological developments and calibration. In *Infrasound Monitoring for Atmospheric*

631   *Studies*, pages 63–89. Springer.

632 [Nishimura et al., 2019] Nishimura, R., Cui, Z., and Suzuki, Y. (2019). Portable infrasound monitoring device

633   with multiple mems pressure sensors. In *International Congress on Acoustics (ICA)*, pages 1498–1505.

634 [Peterson, 1993] Peterson, J. R. (1993). Observations and modeling of seismic background noise. Technical

635   report, US Geological Survey.

636 [Poler et al., 2020] Poler, G., Garcia, R. F., Bowman, D. C., and Martire, L. (2020). Infrasound and gravity

637   waves over the andes observed by a pressure sensor on board a stratospheric balloon. *Journal of Geophysical*

638   *Research: Atmospheres*, 125(6):e2019JD031565.

639 [Ponceau and Bosca, 2010] Ponceau, D. and Bosca, L. (2010). Low-noise broadband microbarometers. In

640   *Infrasound monitoring for atmospheric studies*, pages 119–140. Springer.

641 [Raspet et al., 2019] Raspet, R., Abbott, J.-P., Webster, J., Yu, J., Talmadge, C., Alberts II, K., Collier, S.,

642   and Noble, J. (2019). New systems for wind noise reduction for infrasonic measurements. In *Infrasound*

643   *Monitoring for Atmospheric Studies*, pages 91–124. Springer.

644 [Richiardone, 1993] Richiardone, R. (1993). The transfer function of a differential microbarometer. *Journal*

645   *of Atmospheric and Oceanic Technology*, 10(4):624–628.

646 [Shani-Kadmiel et al., 2018] Shani-Kadmiel, S., Assink, J. D., Smets, P. S., and Evers, L. G. (2018). Seismoa-

647   coustic coupled signals from earthquakes in central italy: Epicentral and secondary sources of infrasound.

648   *Geophysical Research Letters*, 45(1):427–435.

649 [Slad and Merchant, 2016] Slad, G. W. and Merchant, B. J. (2016). Chaparral model 60 infrasound sensor

650   evaluation. *Technical Report*, pages SAND2016–1902.

651 [Sleeman et al., 2006] Sleeman, R., Van Wettum, A., and Trampert, J. (2006). Three-channel correlation

652   analysis: A new technique to measure instrumental noise of digitizers and seismic sensors. *Bulletin of the*

653   *Seismological Society of America*, 96(1):258–271.

654 [Speller and Yu, 2004] Speller, K. E. and Yu, D. (2004). A low-noise mems accelerometer for unattended

655   ground sensor applications. In *Unattended/Unmanned Ground, Ocean, and Air Sensor Technologies and*

656   *Applications VI*, volume 5417, pages 63–72. International Society for Optics and Photonics.

657 [Steinhart and Hart, 1968] Steinhart, J. S. and Hart, S. R. (1968). Calibration curves for thermistors. In

658   *Deep Sea Research and Oceanographic Abstracts*, volume 15, pages 497–503. Elsevier.

659 [STMicroelectronics, 2017] STMicroelectronics (2017). *Technical Report STMicroelectronics LPS33HW*.

660   STMicroelectronics.

661 [STMicroelectronics, 2018] STMicroelectronics (2018). *Technical Report STMicroelectronics LSM303*. STMi-

662   croelectronics.

663 [Sutherland and Bass, 2004] Sutherland, L. C. and Bass, H. E. (2004). Atmospheric absorption in the atmo-

664   sphere up to 160 km. *The Journal of the Acoustical Society of America*, 115(3):1012–1032.

665 [TDK, 2018] TDK (2018). *Technical Report TDK NTC element G1540*. TDK.

666 [Texim Europe, 2013] Texim Europe (2013). *Technical Report Texim Europe GNS2301*. Texim Europe.

667 [Walker and Hedlin, 2010] Walker, K. T. and Hedlin, M. A. (2010). A review of wind-noise reduction method-

668   ologies. In *Infrasound monitoring for atmospheric studies*, pages 141–182. Springer.

669 [Washburn, 1921] Washburn, E. W. (1921). The dynamics of capillary flow. *Physical review*, 17(3):273.

[Waxler and Assink, 2019] Waxler, R. and Assink, J. (2019). Propagation modeling through realistic atmosphere and benchmarking. In *Infrasound Monitoring for Atmospheric Studies*, pages 509–549. Springer.

[Wessel et al., 2013] Wessel, P., Smith, W. H., Scharroo, R., Luis, J., and Wobbe, F. (2013). Generic mapping tools: improved version released. *Eos, Transactions American Geophysical Union*, 94(45):409–410.

[Zirpel et al., 1978] Zirpel, M., Kraan, W., and Mastboom, P.-P. (1978). *Operationele versterkers: een verzameling schakelingen en formules voor de toepassing van operationele versterkers*. Kluwer.

[Zou et al., 2014] Zou, X., Thiruvenkatanathan, P., and Seshia, A. A. (2014). A seismic-grade resonant mems accelerometer. *Journal of Microelectromechanical Systems*, 23(4):768–770.
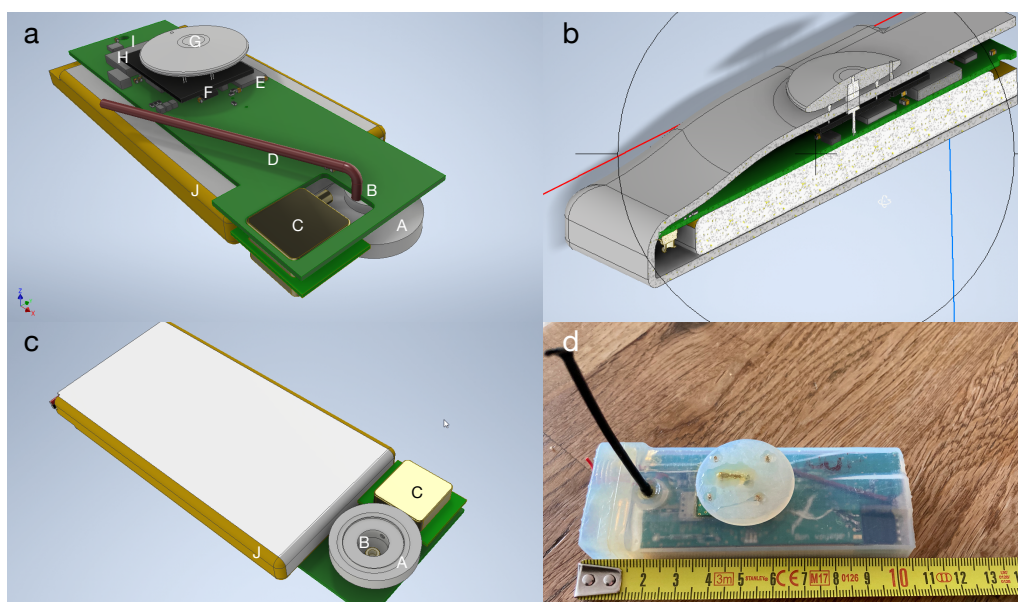
Figure 1: 3D CAD design of (a) the top of the PCB, (b) the casing, (c) the bottom of the PCB with pressure dome, and (d) a picture of the actual platform. The PCB hosts; a pressure dome (a-A/c-A), a barometric pressure sensor (a-B/c-B), a differential pressure sensor (a-C/c-C), a PEEKsil^{TM} Red series capillary (a-D), an accelerometer (a-F), an anemometer (a-F) with heating element (a-G), a microcontroler (a-H), a GPS (a-I), and a lithium battery (a-J/c-J).
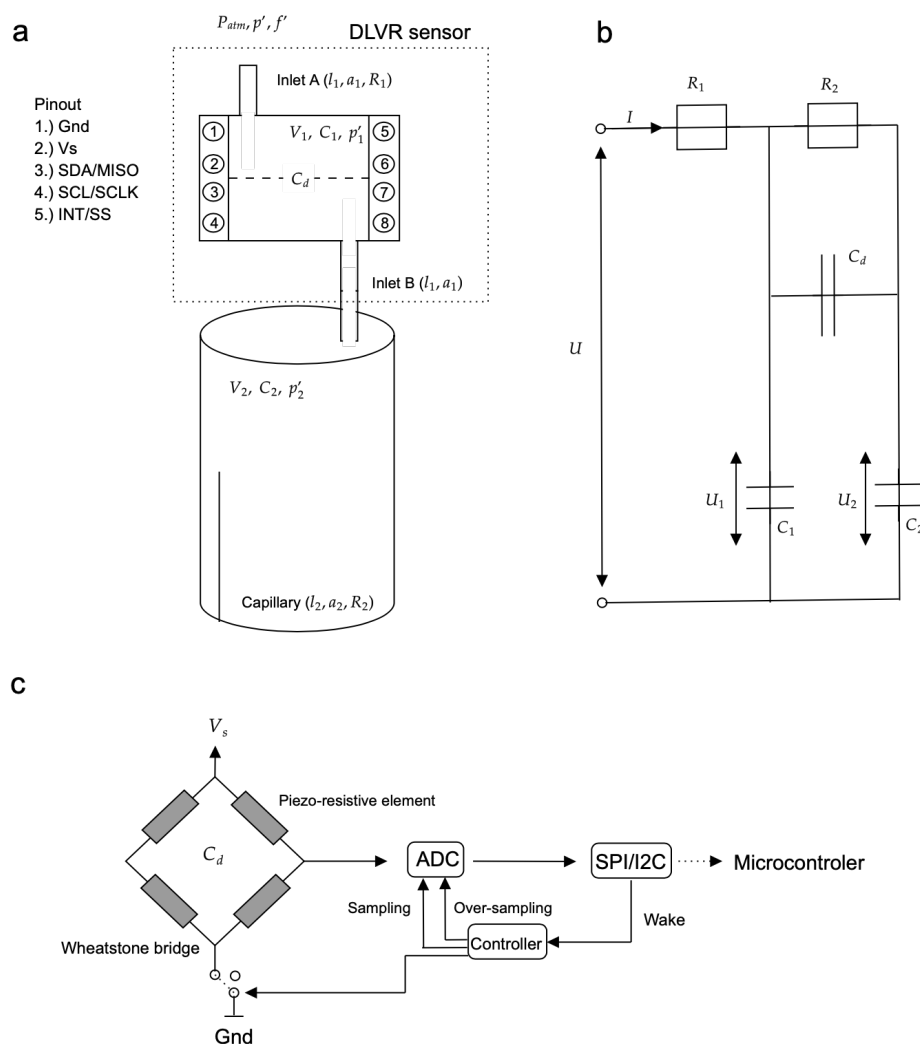
Figure 2: The KNMI mini-MB design with the DLVR sensor and the parameters as listed in Table 1 (a), as well as the electrical circuit of the mini-MB (b). Panel (c) visualises the DLVR sensor.
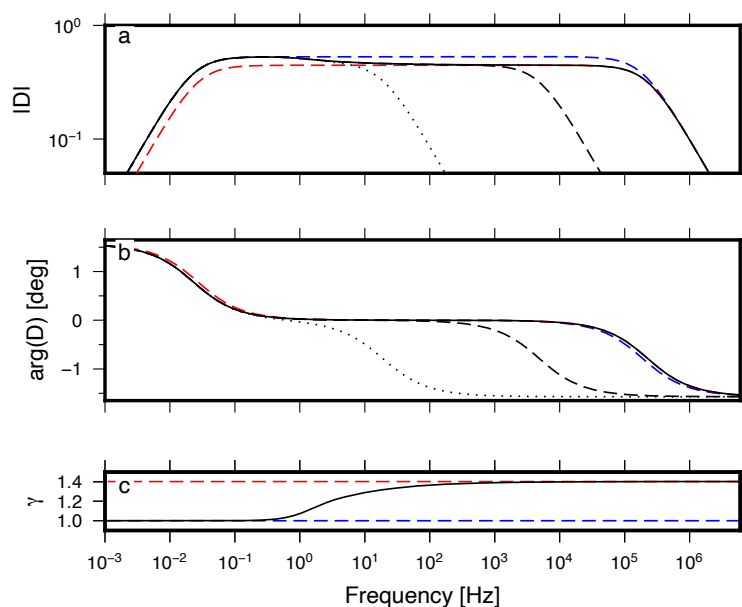
Figure 3: The theoretical sensor frequency response function for (a) amplitude and (b) phase in the case of isothermal and adiabatic gas behaviour in blue and red, respectively. The solid black line indicates the corrected sensor response by $\overline{\gamma}$ (c), as discussed in Section 3.1.3. The dotted and dashed line indicate the shifting high frequency cut-off due to R_{gore}, as discussed in section 3.1.4.
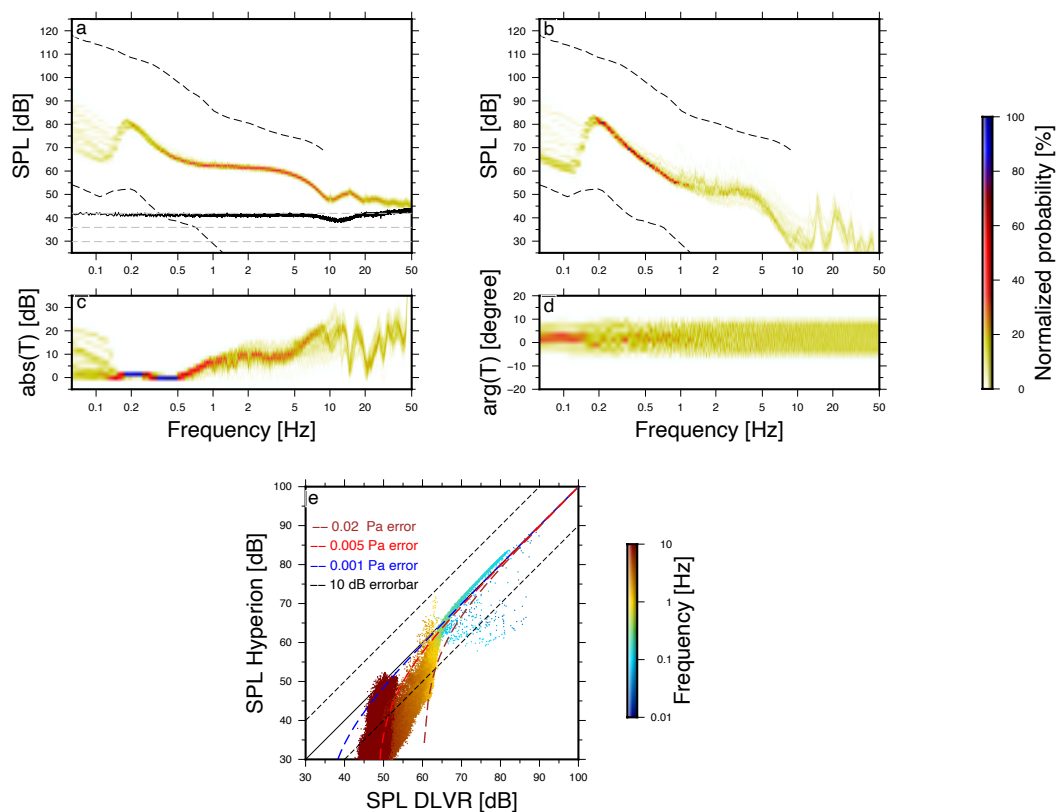
Figure 4: PDF's of pressure spectra recorded with the mini-MB (a) and the Hyperion sensor (b) for a week of continuous recording in dB re. 20^{-6} Pa^2/Hz. The dotted lines indicate the infrasonic high and low ambient noise levels. Panel (a) shows as well the PSD of the 24hr self-noise recording of the mini-MB in black. Panels (c) and (d) visualise the absolute difference T in amplitude and phase between the mini-MB and the Hyperion as a function of frequency. Panel (e) displays the differences in sound pressure level measured by the mini-MB and the Hyperion sensor for the various frequencies.
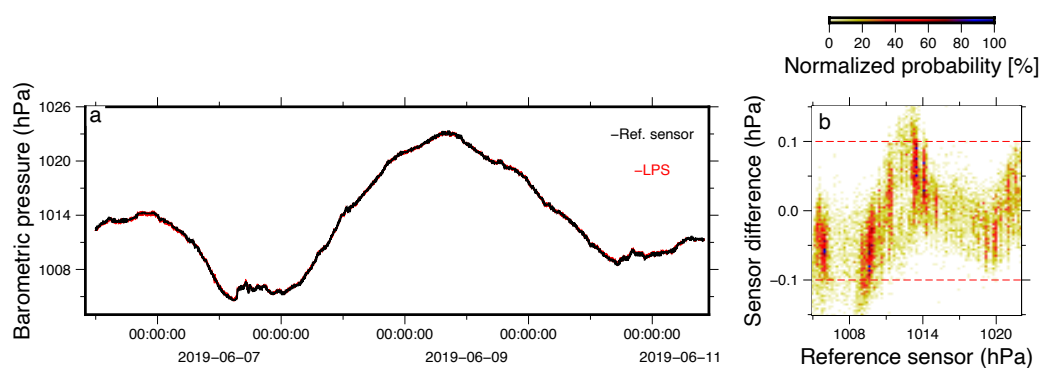
Figure 5: A comparison between the Barometric MEMS sensor (red) and a KNMI reference barometer (black). Panel (a) shows five days of barometric pressure recordings using both sensor, while panel (b) displays the difference in measured barometric pressure by the MEMS and the reference sensor.
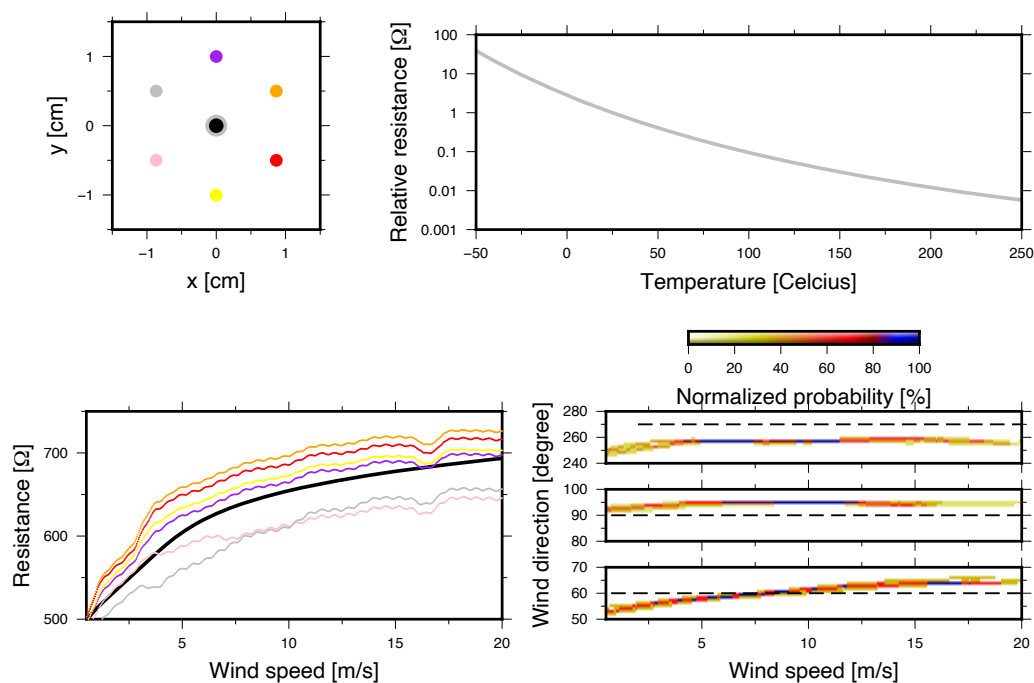
Figure 6: Analyses of the anemometer. Panel a shows the top view of the sensor design, with the central heating element. Panel b indicates the resistivity of the thermistors over temperature. The measured resistance of the thermistors for calibration set-up a, the colors are in agreement with the sensor design (a), are shown in panel c. The solid black line is the average $4th$ order polynomial fit. Panel d indicates the resolved wind direction (solid lines) compared with the expected direction (dotted lines) of set-ups a, b, and c.
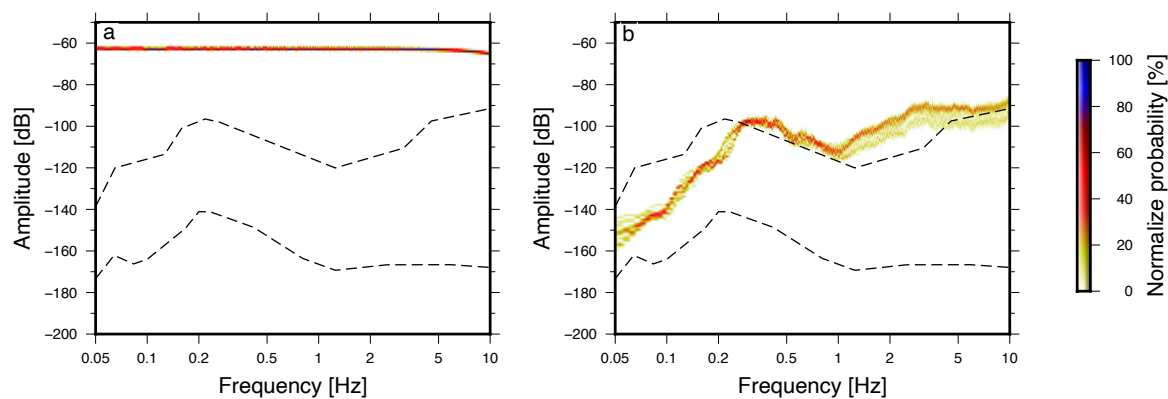
Figure 7: PDF's of the LSM IMU accelerometer (a) and the Streckeisen STS-2 connected to a Quanterra Q330 (b) for 24 hours of continuous recording in dB re. $m^2s^{-4}Hz^{-1}$. The dotted lines indicate the seismic high and low ambient noise levels.